Thermal stress analysis of a planar SOFC stack

Chih-Kuang Lin [a,*], Tsung-Ting Chen [a], Yau-Pin Chyou [b], Lieh-Kwang Chiang [b]

[a] *Department of Mechanical Engineering, National Central University, Jhong-Li 320, Taiwan*
[b] *Nuclear Fuel & Material Division, Institute of Nuclear Energy Research, Lung-Tan 325, Taiwan*

Abstract

The aim of this study is, by using finite element analysis (FEA), to characterize the thermal stress distribution in a planar solid oxide fuel cell (SOFC) stack during various stages. The temperature profiles generated by an integrated thermo-electrochemical model were applied to calculate the thermal stress distributions in a multiple-cell SOFC stack by using a three-dimensional (3D) FEA model. The constructed 3D FEA model consists of the complete components used in a practical SOFC stack, including positive electrode–electrolyte–negative electrode (PEN) assembly, interconnect, nickel mesh, and gas-tight glass-ceramic seals. Incorporation of the glass-ceramic sealant, which was never considered in previous studies, into the 3D FEA model would produce more realistic results in thermal stress analysis and enhance the reliability of predicting potential failure locations in an SOFC stack. The effects of stack support condition, viscous behavior of the glass-ceramic sealant, temperature gradient, and thermal expansion mismatch between components were characterized. Modeling results indicated that a change in the support condition at the bottom frame of the SOFC stack would not cause significant changes in thermal stress distribution. Thermal stress distribution did not differ significantly in each unit cell of the multiple-cell stack due to a comparable in-plane temperature profile. By considering the viscous characteristics of the glass-ceramic sealant at temperatures above the glass-transition temperature, relaxation of thermal stresses in the PEN was predicted. The thermal expansion behavior of the metallic interconnect/frame had a greater influence on the thermal stress distribution in the PEN than did that of the glass-ceramic sealant due to the domination of interconnect/frame in the volume of a planar SOFC assembly.

1. Introduction

Solid oxide fuel cells (SOFCs) utilize solid ceramics as the electrolyte and electrode and operate at high temperatures such that they can provide the highest efficiencies of all fuel cells. Such high operation temperatures also provide flexibility of fuel needed such that hydrogen, carbon monoxide, methane, and some higher hydrocarbons can be used. There are two major configuration designs for SOFC developed, namely, tubular and planar cells. Planar SOFCs are becoming more popular because they are easier to fabricate, operate at a lower temperature, and offer a higher power density relative to the tubular type of SOFC. A typical unit cell in a planar SOFC stack is composed of a positive electrode–electrolyte–negative electrode (PEN) assembly, a porous nickel mesh, two end interconnect plates, and gas seals.

In practical applications of SOFCs, multiple cells are assembled to form a stack and make a serial connection in the electric loop to generate a high voltage and power. The high-temperature operation, however, gives rise to significant thermal stresses due to mismatch of coefficient of thermal expansion (CTE) between components and temperature gradients in the SOFC system. Such thermal stresses can cause delamination and microcracking in the critical layers of the PEN [1] and degrade the SOFC performance. Therefore, a comprehensive thermal stress analysis of the SOFC stack is necessary for the success in design and operation of a SOFC system.

There are a few studies [1–8] in the literature which have investigated the thermal stresses in SOFCs. Some of these studies [1–5] used experimental and/or numerical methods to evaluate the residual stresses in electrolyte and/or electrode layers at room and/or operation temperature by applying a uniform temperature distribution within a simple PEN plate. Those studies [1–5] were mainly focused on the thermal stresses caused only by the mismatch of CTE between the electrolyte and

* Corresponding author. Tel.: +886 3 426 7340; fax: +886 3 425 4501.
  E-mail address: t330014@cc.ncu.edu.tw (C.-K. Lin).

electrode layers for a given temperature change without considering the temperature gradients within the PEN and thermal interactions between PEN and other cell components. Other studies used finite element analysis (FEA) to calculate the thermal stresses by developing and employing coupled thermo-electrochemical models to generate the needed temperature profiles for planar [6,7] and tubular [8] SOFCs. As a result, the contributions of thermal gradients or non-uniform temperature distributions inside the cell to the generation of thermal stress can be included and simulated by such coupled thermo-electrochemical approaches [6–8]. In each of those studies [6–8], a three-dimensional (3D) FEA model of a single unit cell was constructed to calculate the thermal stresses in each component of the unit cell. Note that the FEA models of a single cell for the planar SOFCs investigated in Refs. [6,7] included components like the PEN and interconnect such that the effects of CTE mismatch and mechanical constraint between these two components were also taken into account in the thermal stress simulation. Therefore, simulation approaches like those proposed in Refs. [6,7] would provide a very effective tool for assessment of thermal stress distribution and generate very useful results for design of planar SOFCs. However, in those studies [6,7], for the sake of simplicity in calculation, a single-cell stack model was constructed and cell components such as gas seals were not included in the 3D FEA model. As the planar type of SOFC requires high-temperature gas seals such as glass and glass-ceramic materials to bond the cell components and separate the fuel and air compartments, the influence of the behavior of gas seals on the thermal stress distribution in planar SOFCs also needs to be evaluated. If the thermal stresses in gas seals exceed critical values, failure of gas seals at operation temperature might cause leakage in cells and degrade the efficiency of an SOFC system. However, this important issue still lacks sufficient studies in the literature and provides a need for the current study to investigate the role of the gas seals in the structural stability and durability of planar SOFCs for practical applications.

To provide an effective tool for assessment of thermal stress in a planar SOFC system, it would be better to use a simulation model as close as possible to the practical applications. As described above, the models used in prior work [1–7] on thermal stress analysis of planar SOFCs are simplified to some extent. In particular, a comprehensive 3D model of multiple-cell SOFC stack has not yet been developed to generate more realistic thermal stress analysis results for a practical application. For this reason, a 3D multiple-cell model based on a prototype planar SOFC stack design would be constructed in the current study to perform comprehensive thermal stress analyses.

The purpose of this study is, by using a commercial FEA code, to analyze the thermal stress distributions in a planar SOFC stack during various stages. A 3D FEA model was constructed based on the design of a prototype planar SOFC stack, which is currently under development at the Institute of Nuclear Energy Research (INER), Taiwan. An integrated thermo-electrochemical approach [9] developed at INER was applied to generate the temperature profiles during start-up and

steady-state stages. Subsequently, the resultant temperature profiles were read into the FEA code to carry out the thermal stress calculation. Glass-ceramic sealants which were never considered in previous studies were included in the multiple-cell stack model to produce more realistic results from the thermal stress simulation. Effects of bottom support condition, CTE mismatch, temperature profiles, and viscous behavior of the glass-ceramic sealant were discussed. Such results will help predict the locations that failure may take place during shutdown and operation stages, and help choose suitable sealants and interconnects which should be strong enough for structural stability of the cell stack.

2. Modeling

2.1. Finite element model

Commercial FEA code 'ABAQUS' (ABAQUS Inc., Providence, RI, USA) was used in this study to calculate the thermal stress distributions in a planar SOFC stack during shutdown, transient, and steady-state conditions. The FEA model was constructed based on the stack design of a prototype counter-flow SOFC, which is being developed at INER. A counter-flow configuration was selected because it would produce a greater power density compared to other flow patterns [9]. Because the geometry of the planar SOFC stack is symmetric, only one-half of the stack configuration is needed for a 3D FEA model. In the current study, such a 3D model was constructed for a SOFC stack consisting of three unit cells. Each unit cell is composed of a PEN assembly, two interconnects with gas channels, and a nickel mesh. Fig. 1 is the schematic of one-half of this planar SOFC stack assembly. As shown in Fig. 1, these three unit cells are assembled together to become a three-cell SOFC stack by using glass-ceramic sealants to bond the PEN-supporting frames with the connecting interconnects. Note that glass-ceramic sealants are also used along the edges of the PEN to bond with
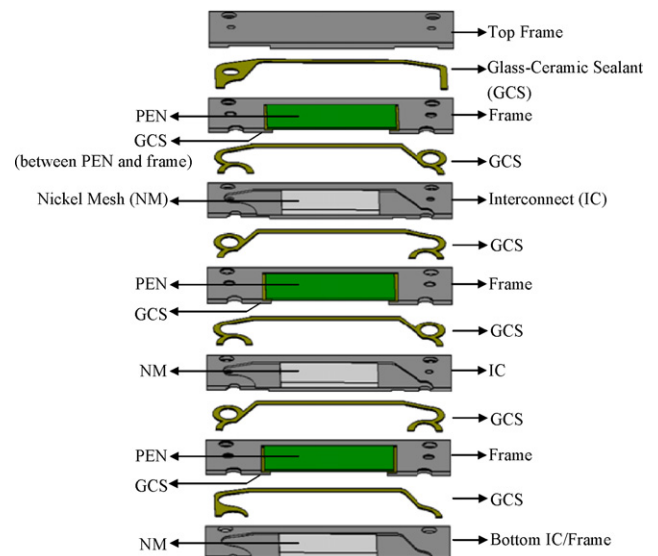

Fig. 1. Schematic of one-half of a planar SOFC stack assembly consisting of three unit cells.
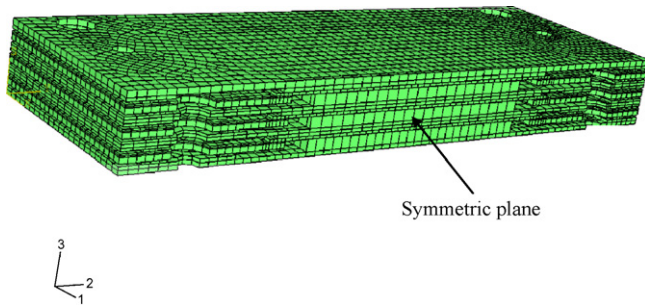
Fig. 2. Schematic of the finite element model for one-half of a three-cell SOFC stack.

the supporting frame. In constructing this 3D model, the gas channels in the interconnects were also included to get a more realistic simulation. The sizes of the PEN and interconnect used here are 80 mm × 80 mm and 150 mm × 100 mm, respectively. The thickness of the PEN was 0.7 mm while the thickness of the interconnect and frame is between 2 and 2.5 mm depending on the location of gas channels and other geometric needs in the plate. As the thickness of each component in the planar SOFC is significantly smaller than the other dimensions, an eight-node continuum shell element (SC8R) [10] was employed in this study. From a modeling point of view, continuum shell elements look like 3D continuum solids, but their kinematic and constitutive behavior is similar to that of conventional shell elements [10]. Fig. 2 shows the discrete meshes of the 3D FEA model constructed for one-half of the three-cell SOFC stack investigated. There are total 30,687 elements and 52,267 nodes in this 3D model. Note that in Figs. 1 and 2, the fuel inlet for this counter-flow planar SOFC is located at the left end of the stack while the air inlet is located at the right end of the stack.

In general, stresses caused by self-weight of SOFC components are relatively small compared to thermal stresses such that they were neglected in this simulation. A "tight-bonding constraint" condition was set between the glass-ceramic seals and connecting components. Contact between cell components, such as: (1) PENs with gas channels of the interconnects, (2) PENs with nickel meshes, and (3) nickel meshes with interconnects, was considered by setting a "contact constraint" condition for these contact pairs in the FEA modeling. The frictional force was neglected in setting such a contact constraint condition. Three boundary conditions were given to analyze the effects of stack bottom support on thermal stress distribution. The given three bottom supports include plane-, edge-, and point-support. In plane-support, the entire bottom surface of the bottom frame was constrained in the direction normal to the bottom plane, i.e. supported over the entire bottom surface by a rigid foundation. In edge-support, the edges of the bottom surface were constrained in the direction normal to the bottom plane, i.e. simply supported at the bottom edges. In point-support, the corner points of the bottom surface were constrained in the direction normal to the bottom plane in a way like a simple support condition. An additional constraint was applied to a edge point on the symmetric plane for all the given support conditions to pre-

vent the rigid body motion of the whole stack model. In these given support conditions, the three-cell SOFC stack was simply assumed to rest on the specified supports without considering any particular joining technique between the bottom surface and each support. Therefore, any effect of the bonded interface or frictional sliding between the bottom surface and each given supporting surface, edge or point was neglected in the current study. In other words, no additional constraint was set against the in-plane motion of the bottom surface except to prevent rigid body motion.

2.2. Material properties

As the operation temperature for the given SOFC is around 800 °C, material properties at such a high temperature are needed to obtain better simulation results. By considering an anode-supported PEN is typically composed of Ni/YSZ cermet structure, temperature-dependent elastic properties of a Ni/YSZ [11] anode was used for the PEN in the present work. An equation describing the relationship between elastic modulus and temperature for such an anode was given in Ref. [11] and employed in the current FEA calculation. As the PEN is basically composed of ceramic materials, it was assumed to deform elastically at both room temperature (RT) and operation temperature. Table 1 is the temperature-dependent tensile properties of Crofer 22-APU used as the frame and interconnect. These properties were obtained by conducting tensile tests in house using plate-type specimens. The obtained engineering stress–strain curves of Crofer 22-APU at different temperatures (Fig. 3) revealed that the tensile strength and elastic modulus were decreased with increasing temperature. Although only a portion of the stress–strain curve data (with strain less than 10%) were shown in Fig. 3, the complete true stress–strain curve data were imported into the FEA calculation. In the FEA calculation, plastic deformation was allowed for the interconnect and frame at both RT and operation temperature.

The elastic properties of G-18 (a barium–calcium aluminosilicate glass-ceramic material) given in Refs. [12,13] were used for the gas seals in the current study. The elastic modulus at RT [13]
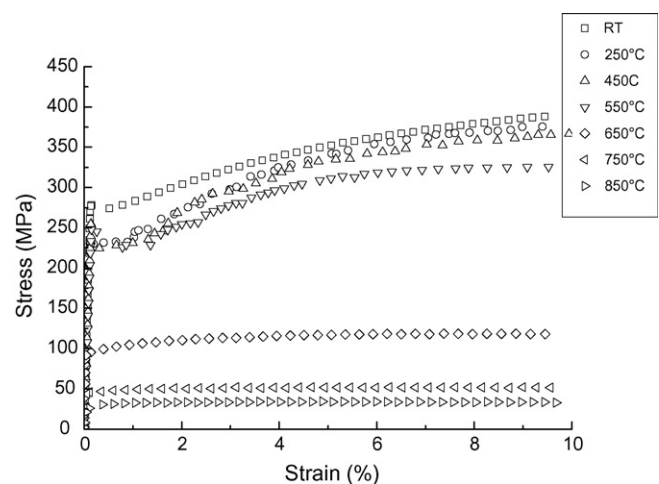

Fig. 3. Engineering stress–strain curves of Crofer 22 at different temperatures.

Table 1
Tensile properties of Crofer 22-APU

Temperature (°C)	Poisson's ratio	Elastic modulus (GPa)	Yield strength (MPa)	True fracture strength (MPa)
25	0.3	216	268	488
250	0.3	210	231	430
450	0.3	201	255	428
550	0.3	184	247	373
650	0.3	124	89	134
750	0.3	92	47	59
850	0.3	48	28	37

and 800 °C [12] is 72 and 10.8 GPa, respectively. According to the slopes of the initial linear portion of the load–displacement curves at 600 and 800 °C in Ref. [12], it was then estimated that the elastic modulus at 600 °C was 21.6 GPa. A Poisson's ratio of 0.3 [12] was used for G-18 sealant at all given temperatures. As shown in Ref. [12], the load–displacement curves for G-18 were linear until failure for temperature up to 700 °C, while the response became nonlinear for temperature higher than 700 °C such that inelastic deformation was considered for gas seals at temperatures above 700 °C in the current FEA calculation. The stress–strain curve for non-aged G-18 at 800 °C given in Ref. [12] was implemented in the current FEA calculation for simulation of the inelastic behavior of the gas seal at operation temperature. Generally, glass-ceramics will become viscous when the temperature is higher than their transition temperature, T_g, so that stresses might be relaxed under such a condition. The T_g of G-18 sealant is 619 °C [13]. In order to investigate the effect of stress relaxation due to the viscous characteristics of the glass-ceramic sealant at operation temperature, it was assumed that the elastic modulus of G-18 at 800 °C was reduced to one-third of the unrelaxed value after the stress relaxation process was completed.

Based on measurement of the density of the nickel mesh used in the given prototype planar SOFC, the elastic modulus of the nickel mesh was obtained by assuming that there is 95 vol.% of porosity in the nickel mesh such that 5% of the elastic modulus of bulk nickel was used for the nickel mesh. The elastic modulus of nickel decreases with increasing temperature at a rate of 0.003675 GPa °C^{-1} [14]. It was therefore assumed that the elastic modulus was decreased from 9.9 to 7.1 GPa [14,15] when the nickel mesh was heated from 25 to 800 °C. In the FEA calculation, the nickel mesh was assumed to deform elastically at both RT and operation temperature due to its great flexibility with small induced thermal stresses. Fig. 4 shows the variation of thermal expansion with temperature for each component. In Fig. 4, the curves of PEN and Crofer 22-APU were obtained by conducting in-house measurements at INER while the curves of G-18 sealant and nickel mesh were taken after Refs. [13,15], respectively.

2.3. Temperature profiles

To solve the transient and steady-state thermal stress distribution after start-up (beginning of the electrochemical reactions), temperature profiles at different stages are needed. Before start-up, the SOFC was uniformly preheated from RT to 600 °C by means of hot inlet fuel and air with a temperature of 640 °C. The transient and steady-state temperature profiles were generated through an approach combining electrochemical and heat-transfer analyses developed at INER [9] using a three-cell stack model. The calculation procedure integrated the electrochemical reactions of the SOFC with FEA models for thermo-mechanical analyses of the interconnect through iteration processes, so that a unified temperature distribution with heat loss effect was obtained [9]. In calculating the temperature profiles for this three-cell stack model, a two-layered ceramic insulation envelope was used to enclose the entire stack and acted as a heat-transfer buffer between the stack and atmospheric air [9]. Details of this integrated thermo-electrochemical approach can be seen in Ref. [9]. Once the transient and steady-state temperature profiles in the entire three-cell stack were determined, the thermal stress calculation was subsequently conducted by importing these temperature profiles into the 3D FEA model. Fig. 5 shows the obtained steady-state temperature profiles for the three-cell stack model with the highest temperature around 800 °C. As shown in Fig. 5, the temperature profiles in the top, middle, and bottom cells are of little difference with the middle one having a slightly larger high-temperature region near the fuel-inlet end (the left end in Fig. 5). It was also seen in Fig. 5 that the in-plane temperature gradients were much larger than the cross-plane gradients in each component layer such that the temperature gradient through the thickness in each component layer was neglected.
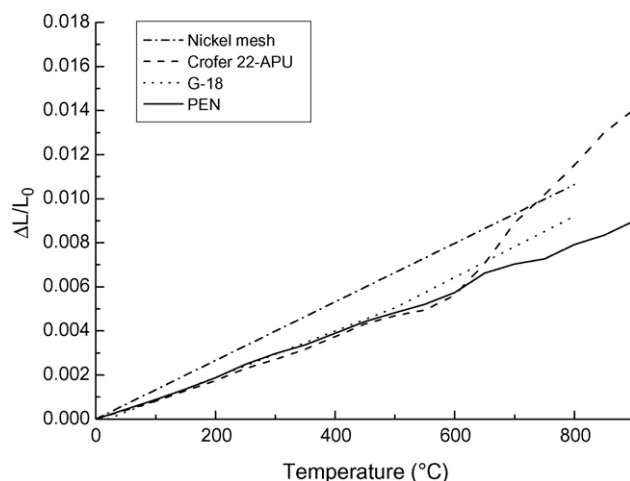

Fig. 4. Thermal expansion behavior of planar SOFC components. (Data for curves of G-18 and nickel mesh were taken from Refs. [13,15], respectively.)
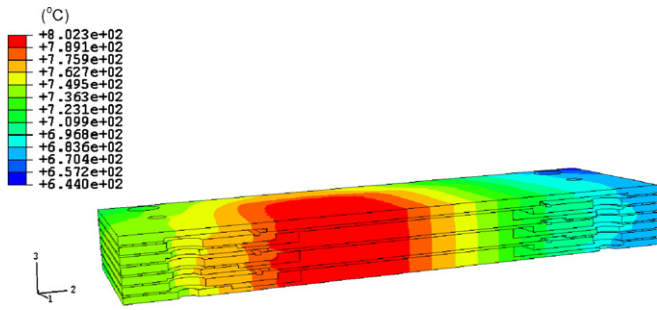
Fig. 5. Temperature distribution at the steady-state condition in a three-cell SOFC stack model.

The in-plane temperature gradients for the top frame of the three-cell stack model are shown in Fig. 6 as an example of the variation of temperature profile with time after start-up in a component layer of this SOFC stack. A current density of $640 \, mA \, cm^{-2}$ in the cells was assumed in calculating these temperature profiles after starting the electrochemical reactions. It can be seen that the temperature distribution has almost reached steady-state in about 6 min after start-up, based on the simulation results shown in Fig. 6. Note that in Fig. 6(f) the in-plane temperature distribution at steady-state is unsymmetrical and the

highest-temperature region is located at the lower half of this figure. The unsymmetrical, non-uniform temperature distribution is mainly due to two reasons: (1) heat generated by chemical reactions is most intense near the fuel inlet and (2) airflow is most effective at cooling near the air inlet [9]. In each figure shown in Fig. 6, the fuel inlet is at the bottom end and the air inlet is at the top end. Detailed discussion on the temperature patterns at steady operation for this SOFC stack design is given elsewhere [9].

2.4. Investigated cases

Cell components are usually assembled together to form a multiple-cell SOFC stack at a high temperature above 800 °C by using glass-ceramic sealants. At such a high temperature in assembling the SOFC stack, the glass-ceramic sealants become viscous and proceed with a chemical reaction to bond the connecting components under a uniform temperature distribution so that an assembling temperature of 800 °C is defined as the initial stress-free condition in the current study. After the assembling process, the multiple-cell stack is then cooled down to RT, which is defined as the shutdown stage hereafter. In this regard, in each of the following investigated cases, the residual stresses in the SOFC stack at shutdown stage before start-up will be first calculated by considering the temperature drop from 800 °C of the initial stress-free condition to RT. These residual stresses at RT are considered in the subsequent steps of thermal stress calculation. The SOFC stack is then preheated to 600 °C before starting the electrochemical reactions. Therefore, the sequence of the temperature profiles imported to the FEA code in the current study takes the following order: (1) uniform distribution at 800 °C, (2) uniform distribution at RT, (3) uniform distribution at 600 °C, and (4) temperature gradients after start-up of the cell operation from 600 °C. Fig. 7 shows the analysis procedure in the present work.
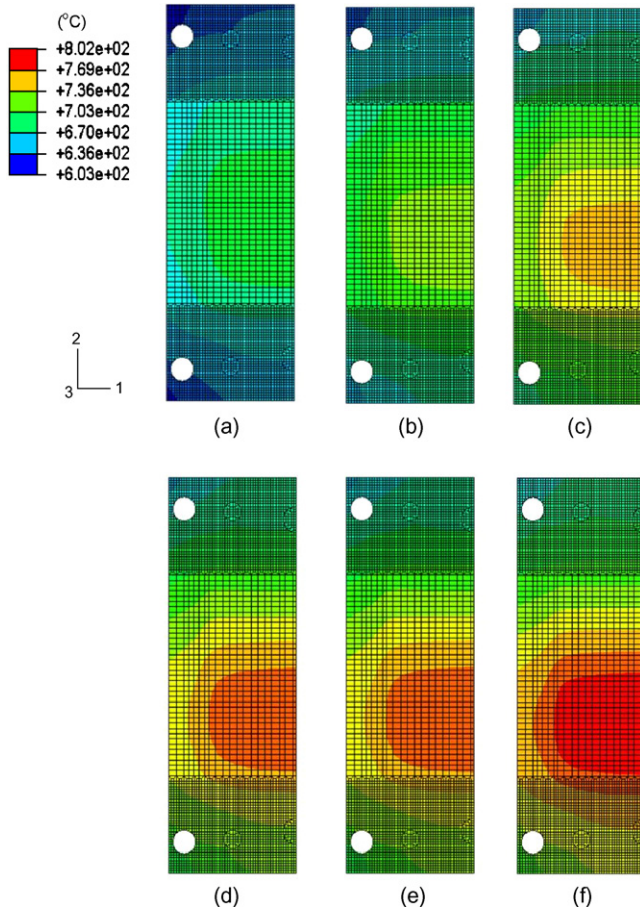

Fig. 6. In-plane temperature profiles on the top frame of a three-cell SOFC stack model after: (a) 30 s, (b) 1 min, (c) 2 min, (d) 6 min, and (e) 14 min from start-up, and at (f) steady-state condition. (Note that fuel and air inlets are located at the bottom and top ends, respectively, in each figure.)
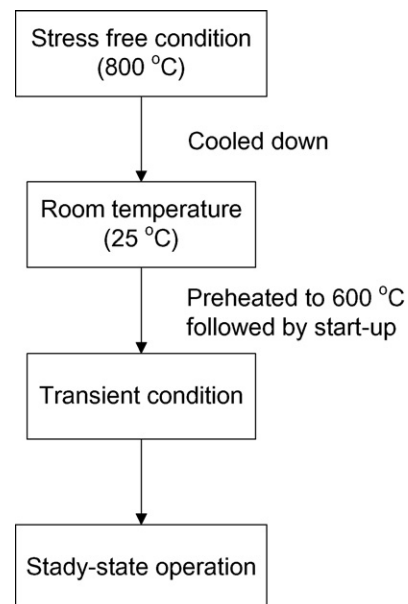

Fig. 7. Analysis procedure of thermal stress distribution.

The investigated cases in the present work include various combinations of boundary conditions, transient and steady-state stages, material properties and other factors. As described above, three kinds of mechanical boundary conditions were assumed at the bottom support and each of them was evaluated using the analysis procedure shown in Fig. 7 such that the thermal stress distributions at RT and after start-up were calculated to study the bottom support effect. As the edge-support has a closer resemblance in simulation to the design of the support for the SOFC stack being developed at INER, it was chosen as the bottom support for analysis of other effects such as temperature gradients and CTE mismatch between components. The CTE of all components were set the same when investigating the effect of temperature gradients alone. Different extents of CTE mismatch of the glass-ceramic sealant and metallic interconnect/frame with respect to the PEN were also assumed to study the CTE mismatch effect on the thermal stress distribution for the given planar SOFC stack design.

2.5. Failure criteria

No matter when the PEN is at RT or operation temperature, the ceramic materials are brittle. Hence, failure of the PEN is defined when the maximum principal stress (MPS) exceeds the ultimate tensile strength of the material. The average strength of an anode-supported PEN is 187 MPa, as measured at RT using ball-on-ring biaxial flexure testing [11]. As given in Ref. [16], the fracture stress of an oxidized anode was decreased about 40% when it was reduced at 800 °C. As an anode-supported PEN is primarily composed of anode material, the strength of PEN was accordingly assumed to be decreased from 187 MPa at RT to 112 MPa at 800 °C. The metallic interconnect/frame is ductile at RT and operation temperature such that notable plastic deformation will occur if the Tresca equivalent stress (TES) exceeds the yield strength of Crofer 22-APU. Note that TES is defined as twice the maximum shear stress at a point [17]. The yield and tensile strength of Crofer 22-APU at different temperatures are tested in house and listed in Table 1. In the current FEA model, plastic deformation of the metallic interconnect/frame was allowed to take place once the stress reached the yield strength. The functions of the nickel mesh are to provide electrical conduction between electrode and interconnect and to act as a gas channel. The stresses in the nickel mesh were calculated but failure of this part was not considered due to its great flexibility leading to small thermal stresses.

As glass-ceramics are brittle at RT but tend to exhibit a nonlinear response at the temperature above T_g, two different criteria were applied to define the failure of glass-ceramic sealants at RT and operation temperature. Failure of the glass-ceramic sealant at RT was defined when the MPS exceeded the tensile strength while Tresca criterion was applied at operation temperature. The flexural strength of G-18 sealant obtained by four-point bending at RT [18] and 800 °C [12] is 48 and 36 MPa, respectively, while the shear strength at 800 °C is 20 MPa [12]. In the analysis procedure, the thermal stress distribution in each SOFC stack component was first determined by the FEA model and then

the critical stress values were compared with the corresponding material strength according to the aforementioned criteria.

3. Results and discussion

3.1. Stress fields at different stages and bottom support conditions

In practical applications of SOFCs, different constraints may be applied to support the cell stack. In this study, three support conditions at the bottom frame of the cell stack were applied. In order to illustrate the effect of bottom support, the calculated stress distribution for each component at such three support conditions was presented individually. Only the maximum principal or shear stresses, hereafter also called the critical stresses, in each component of the entire three-cell stack were identified and discussed. Fig. 8 shows the distributions of maximum in-plane principal stress (MIPPS) in the PENs at RT under three different support conditions after cooling down from the assembling temperature 800 °C. Generally speaking, edges of the PENs were the regions having higher MIPPSs and their values were higher than 120.7 MPa, as shown in Fig. 8. Note that these edge areas of the PEN are tightly bonded with the connecting glass-ceramic sealant. As the temperature fields at both the assembling temperature 800 °C and RT were assumed a uniform distribution without any temperature gradient, the stress fields shown in Fig. 8 were essentially due to CTE mismatch
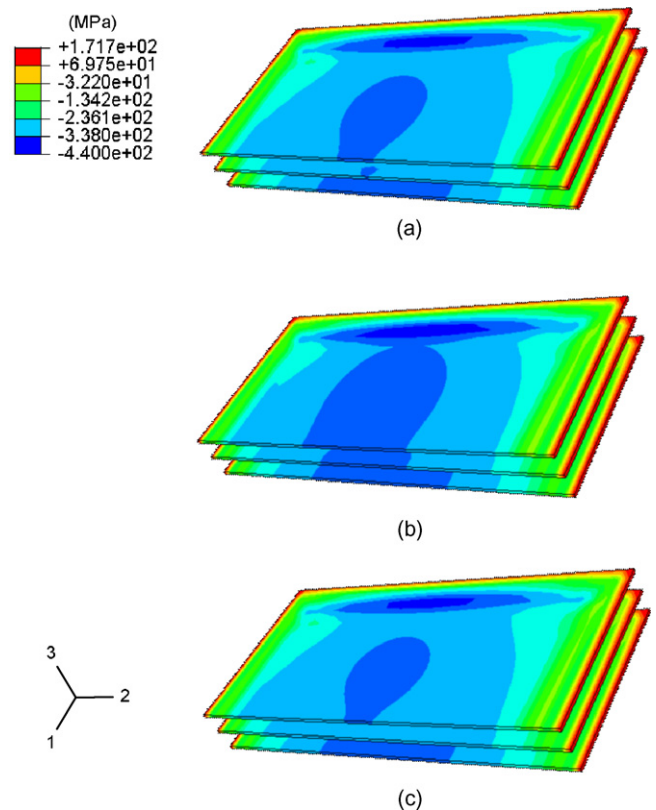

Fig. 8. Distribution of maximum in-plane principal stress in PENs at RT for: (a) edge-support, (b) plane-support, and (c) point-support.

between components. The most highly stressed region in each PEN layer appeared at the corners. The greatest MIPPSs in the PEN at RT for edge-, plane-, and point-support were 171.6, 169.4, and 171.7 MPa, respectively. These values were lower than the average strength 187 MPa at RT [11]. Because of a high scattering of strength for ceramic materials, these MIPPSs at the corners were sufficiently high to be watched. As shown in Fig. 8, the given three support conditions generated comparable stress distributions indicating a change in the bottom support for the given planar SOFC stack did not significantly change the thermal stress distribution at the RT condition. This is due to that only the bottom frame was constrained in different ways and similar constraints were set on the other corresponding components in the three-cell SOFC stack under different support conditions. Fig. 9 shows the distributions of MIPPS in the PENs at steady operation under three different support conditions. Again, equivalent results were obtained for such three boundary conditions at steady operation. The greatest MIPPS, which occurred near the bonding region close to the fuel-inlet end, was 66.82, 69.57, and 68.16 MPa for edge-, plane-, and point-support, respectively. These values were much lower than the estimated strength 112 MPa at 800 °C. Note that the stress fields shown in Fig. 9 were induced by the effect of CTE mismatch as well as temperature gradients at steady operation. As a result, higher MIPPSs took place only at the bonding region near the fuel-inlet end at steady operation (Fig. 9) rather than around all of the edges like that in Fig. 8. Note that the fuel inlet is located at the left end

Fig. 10. Distribution of maximum in-plane principal stress in glass-ceramic sealants at RT for: (a) edge-support, (b) plane-support, and (c) point-support.

while the air inlet is located at the right end in each figure of Figs. 8 and 9 as well as in the following stress distribution figures. It is also seen in Fig. 9 that for each given bottom support condition, the stress distributions at steady operation among the three PENs look somewhat different in color at the areas near the bottom end (symmetric plane). The effect of cell position on the thermal stress distribution will be discussed in the next section.

Fig. 10 shows the distributions of MIPPS in the glass-ceramic sealants at RT after cooling down from the assembling temperature 800 °C. Again, the stress distributions in the glass-ceramic sealants at all given bottom support conditions were also very similar. The greatest MIPPSs occurred at the inner corners of the interior glass-ceramic sealants, which were used to bond the PENs and frames, and had the values of 20.37, 13.77, and 20.31 MPa for edge-, plane-, and point-support, respectively. These values were lower than the flexural strength 48 MPa at RT [18]. For the exterior glass-ceramic sealants connecting interconnects and PEN-supporting frames, they were always subjected to compressive stresses, as the contraction of Crofer 22-APU was much greater than that of G-18 when they were cooled down from the stress-free temperature 800 °C to RT. As described above, glass-ceramic sealants become viscous and exhibit a nonlinear response at operation temperature; Tresca criterion is accordingly employed for failure analysis. Fig. 11 shows the distributions of TES in the glass-ceramic sealants at steady operation. The greatest TES was about 65 MPa for each given support condition and took place at the corners of the interior glass-ceramic sealants near the air-inlet end, as shown in Fig. 11. A TES value of 65 MPa is equal to a maximum shear stress of 32.5 MPa. The corresponding temperature at these highest-shear-stress regions was about 700 °C. The shear strength of G-18 sealant at 800 °C is 20 MPa [12]. Although there is lack of directly experimental data, the shear strength of
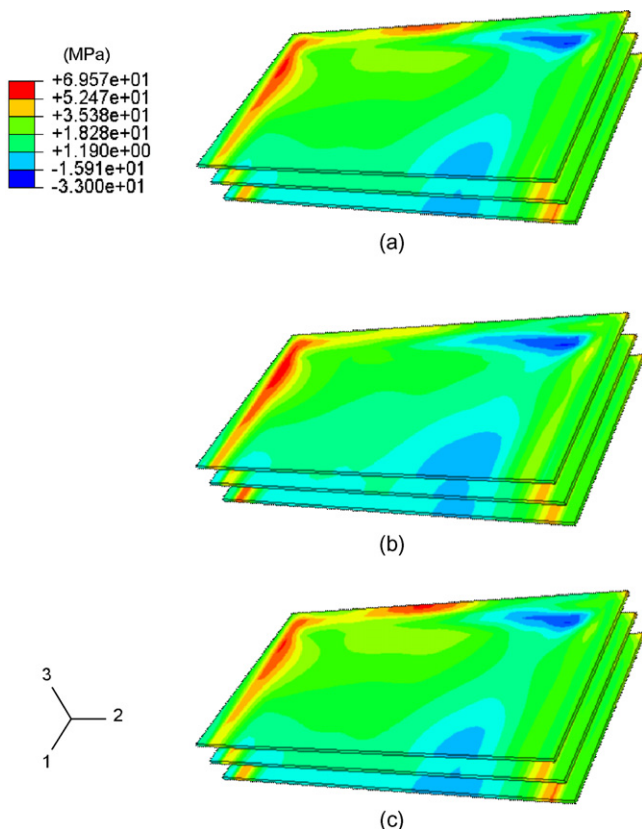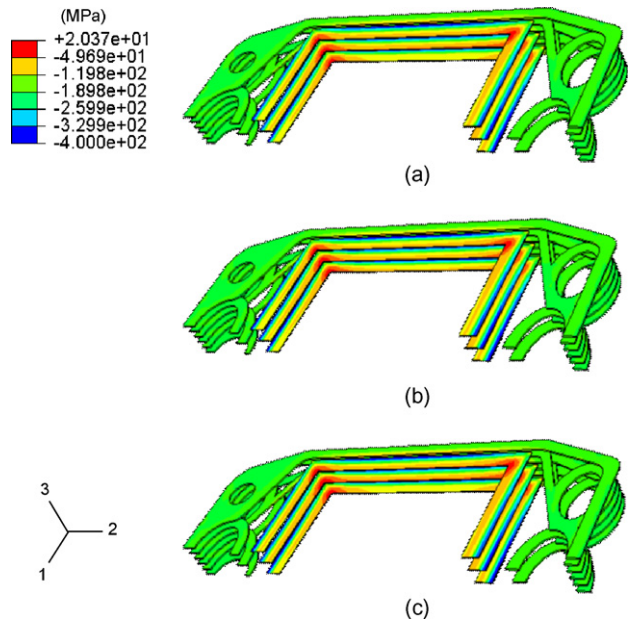

Fig. 9. Distribution of maximum in-plane principal stress in PENs at steady operation for: (a) edge-support, (b) plane-support, and (c) point-support.
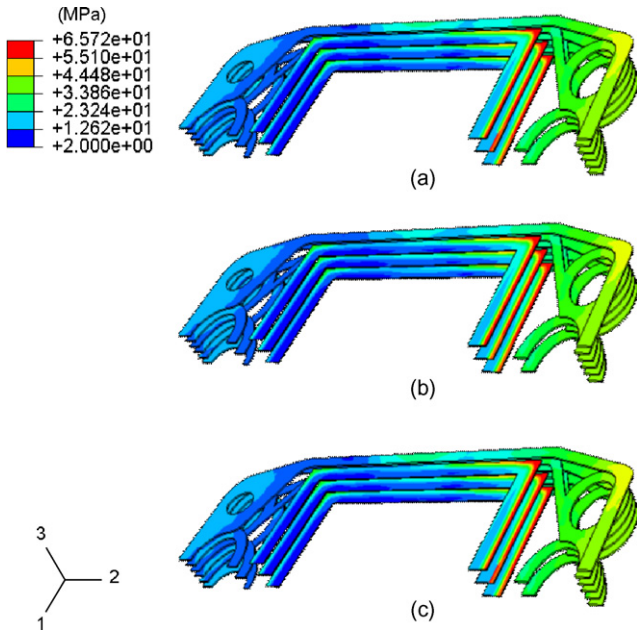
Fig. 11. Distribution of Tresca equivalent stress in glass-ceramic sealants at steady operation for: (a) edge-support, (b) plane-support, and (c) point-support.

Fig. 12. Distribution of Tresca equivalent stress in interconnects and frames at RT for: (a) edge-support, (b) plane-support, and (c) point-support.

G-18 at 700 °C was estimated to be in the range of 20–27 MPa based on the limited data given in Refs. [12,18]. In this regard, the calculated maximum shear stress is presumably greater than the corresponding shear strength of G-18 such that shear fracture of the glass-ceramic sealant at these regions is likely to occur at steady operation. However, further experimental verification for this issue is needed. On the other hand, selection of a stronger gas seal would be an alternative for the current planar SOFC stack design.

Fig. 12 shows the distributions of TES in the interconnects and frames at RT. The greatest TES for the given three support conditions varied from 318.5 to 321.3 MPa and exceeded the yield strength of Crofer 22-APU at RT (Table 1) such that large plastic deformation could take place at the highest-stress regions in the interconnects and frames. The maximum shear strains obtained for the interconnects and frames at RT were 1.88, 1.80, and 1.88% for the edge-, plane-, and point-support, respectively, indicating a considerable plastic deformation at these regions. Therefore, the cooling rate at practical applications should be kept low enough when cooling the SOFC stack from the assembling temperature such that annealing of the metallic interconnect/frame could occur. Such an annealing procedure might reduce a certain extent of residual stress in the interconnect/frame at RT. Fig. 13 shows the distributions of TES in the interconnects and frames at steady operation. The greatest TES varied from 83.01 to 83.27 MPa for the given three support conditions and the corresponding temperature at these areas was about 710 °C. By means of interpolating the tensile test data between 650 and 750 °C in Table 1, it could be seen that such maximum TESs had exceeded the estimated yield strength of Crofer 22-APU at 710 °C (65 MPa) so that considerable plastic deformation might occur at these regions in the interconnects/frames at steady operation. This can also be

evidenced by the calculated maximum shear strains for the interconnects and frames at steady operation which had the values of 1.53, 1.34, and 1.56% for the edge-, plane-, and point-support, respectively.
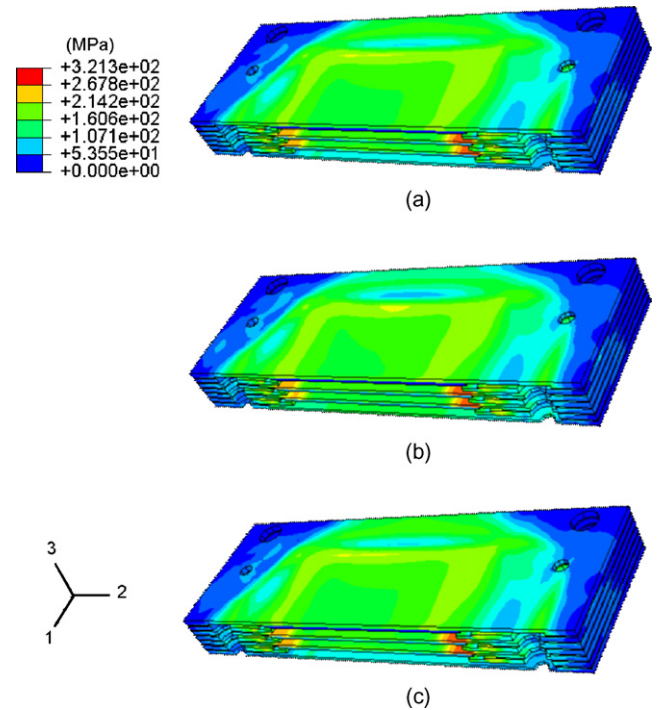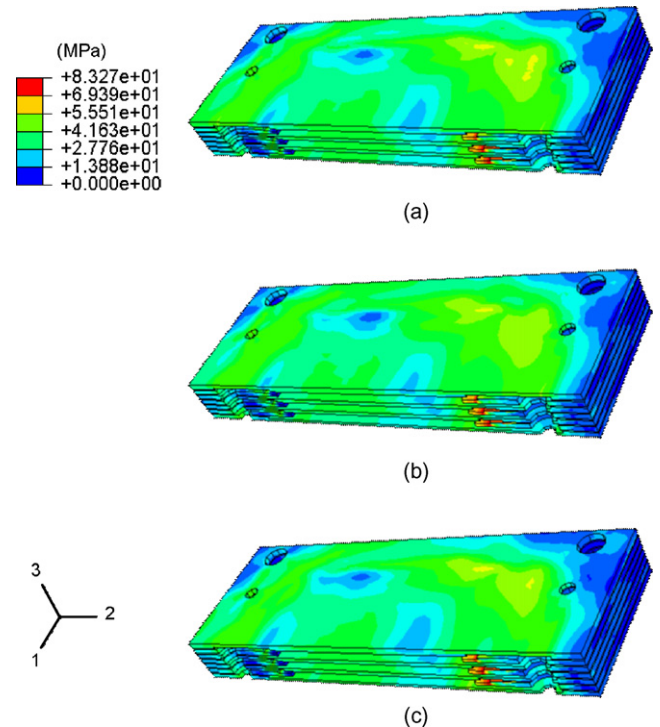

Fig. 13. Distribution of Tresca equivalent stress in interconnects and frames at steady operation for: (a) edge-support, (b) plane-support, and (c) point-support.

Table 2
Critical stresses at edge-support condition

Stage	PEN	Nickel mesh	IC[a]/frame	Glass-ceramic sealant	
	Maximum in-plane principal stress (MPa)	Maximum Tresca equivalent stress (MPa)	Maximum Tresca equivalent stress (MPa)	Maximum in-plane principal stress (MPa)	Maximum Tresca equivalent stress (MPa)
Shutdown	171.6	17.44	318.5	20.37	–
Start-up					
30 s	107.1	24.32	107.4	16.40	–
1 min	87.77	18.55	90.53	26.00	–
2 min	71.37	15.18	89.07	25.39	–
6 min	67.97	13.27	83.95	–	71.01
14 min	68.01	13.21	83.84	–	70.10
Steady-state	66.82	12.11	83.27	–	65.72

[a] IC: interconnect.

Table 3
Critical stresses at plane-support condition

Stage	PEN	Nickel mesh	IC/frame	Glass-ceramic sealant	
	Maximum in-plane principal stress (MPa)	Maximum Tresca equivalent stress (MPa)	Maximum Tresca equivalent stress (MPa)	Maximum in-plane principal stress (MPa)	Maximum Tresca equivalent stress (MPa)
Shutdown	169.4	16.25	321.3	13.77	–
Start-up					
30 s	108.1	19.38	108.7	13.60	–
1 min	88.66	14.43	96.49	22.60	–
2 min	72.11	12.08	92.85	22.22	–
6 min	69.43	10.62	87.49	–	70.97
14 min	69.22	10.58	87.38	–	70.09
Steady-state	69.57	9.859	83.13	–	65.59

Thermal stress distribution in each component of the three-cell stack model during the transient start-up stage was also calculated. Instead of showing the detailed stress fields in each component during the start-up stage, only the critical stress values were listed in Tables 2–4 for the given three support conditions. Note that the aforementioned results at RT (shutdown stage) and steady operation were also included in Tables 2–4 for comparison. As seen in Tables 2–4, for each cell component under a given bottom support condition, each of the compared critical stresses was generally decreased with increasing time after the electrochemical reactions started up until reaching a steady-state. This is due to the fact that the steady-state has the smallest temperature differences from the initial stress-free temperature 800 °C compared to the shutdown and transient start-up stages. Again, as seen in Tables 2–4, the given three support conditions resulted in comparable critical stress values at each transient stage after start-up. In this regard, support condition at the bottom frame did not significantly influence the thermal stress distribution in the three-cell stack. In the following discussion, only the edge-support condition was applied to investigate other effects on the thermal stress distribution in the planar SOFC stack.

Table 4
Critical stresses at point-support condition

Stage	PEN	Nickel mesh	IC/frame	Glass-ceramic sealant	
	Maximum in-plane principal stress (MPa)	Maximum Tresca equivalent stress (MPa)	Maximum Tresca equivalent stress (MPa)	Maximum in-plane principal stress (MPa)	Maximum Tresca equivalent stress (MPa)
Shutdown	171.7	17.48	318.5	20.31	–
Start-up					
30 s	106.8	24.53	106.8	16.75	–
1 min	87.52	18.76	97.07	26.35	–
2 min	71.13	15.42	93.06	25.71	–
6 min	69.20	13.50	87.68	–	71.01
14 min	69.20	13.45	87.57	–	70.12
Steady-state	68.16	12.34	83.01	–	65.72

Table 5
Critical stresses for top, middle, and bottom cells in a three-cell stack

Stage	Cell position	PEN	Nickel mesh	IC/frame	Glass-ceramic sealant	
		Maximum in-plane principal stress (MPa)	Maximum Tresca equivalent stress (MPa)	Maximum Tresca equivalent stress (MPa)	Maximum in-plane principal stress (MPa)	Maximum Tresca equivalent stress (MPa)
Shutdown	Top	171.6	17.44	318.5	13.01	–
	Middle	169.8	15.53	303.6	20.14	–
	Bottom	167.0	12.77	303.9	20.37	–
Steady-state	Top	65.36	9.252	79.86	–	65.59
	Middle	64.13	9.783	82.01	–	65.08
	Bottom	66.82	12.11	83.27	–	65.59

3.2. Effect of cell position

As the 3D SOFC stack model constructed in the current study is composed of three unit cells, it is worth discussing whether there is any significant difference in the thermal stress distribution among these three unit cells. In the following discussion, each of the top, middle, and bottom cell in the three-cell stack is composed of a complete set of cell components including PEN, interconnect/frame, nickel mesh, and glass-ceramic sealant. Table 5 shows the critical stresses in the top, middle, and bottom unit cell under an edge-support condition. The greatest MIPPS in the PEN of each unit cell either at RT or steady operation was very close to each other (Table 5), while a slight difference in the stress distribution pattern from cell to cell was observed, particularly, at the low-stress regions, as shown in Figs. 14 and 15. When the SOFC stack was cooled from 800 °C to RT, the greatest MIPPS in the top PEN was slightly larger than those in the middle and bottom ones. However, the location with

the greatest MIPPS in the PEN was moved to the bottom PEN at steady operation. The greatest TES in the interconnect/frame at RT occurred in the top cell and the value was 318.5 MPa which was slightly greater than those in the middle and bottom cells. After the SOFC reached the steady-state stage, the location with the greatest TES in the interconnect/frame was shifted to the bottom cell but the values in all of the three cells were of little difference. For the glass-ceramic sealants, the greatest MIPPS at RT took place at the bottom cell and the greatest TES at the steady-state in each cell was almost the same, as shown in Table 5.

In general, for a given stage, the thermal stress distribution in a corresponding component differs slightly among the cells in the three-cell SOFC stack, for example, as shown in Figs. 14 and 15 for the PENs. Nevertheless, for a corresponding component at a certain stage, the highest-stress regions in the top, middle, and bottom cells were almost at the same location and the corresponding critical stress values are comparable as shown in
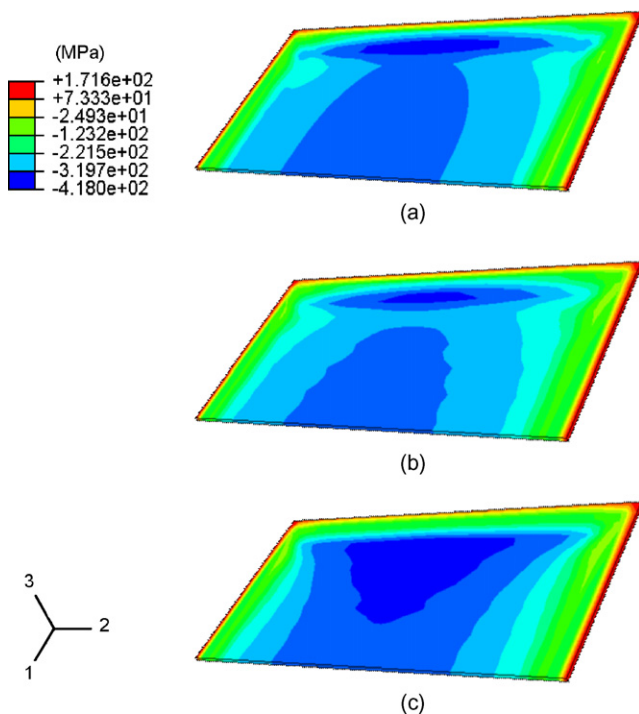

Fig. 14. Distribution of maximum in-plane principal stress in the PEN at RT for the (a) top, (b) middle, and (c) bottom cells.
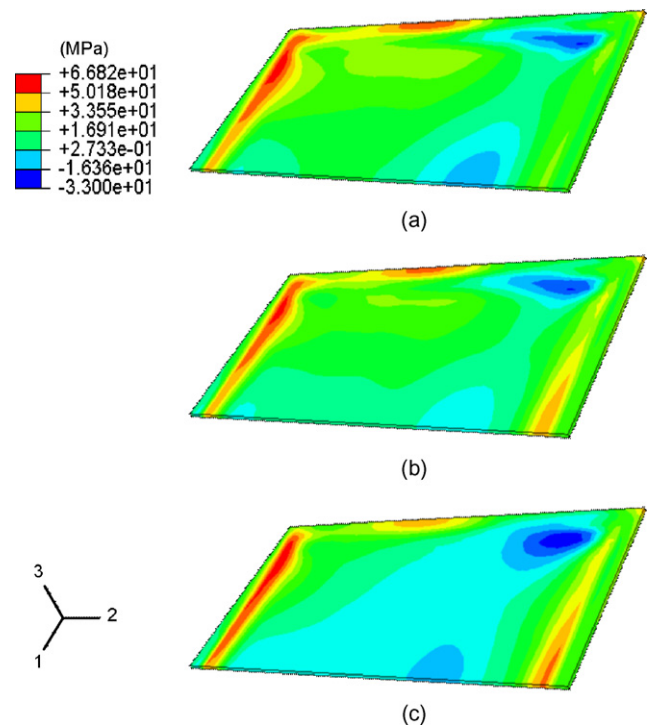

Fig. 15. Distribution of maximum in-plane principal stress in the PEN at steady operation for the (a) top, (b) middle, and (c) bottom cells.

Table 6
Critical stresses caused by steady-state temperature gradients alone

PEN	Nickel mesh	IC/frame	Glass-ceramic sealant
Maximum in-plane principal stress (MPa)	Maximum Tresca equivalent stress (MPa)	Maximum Tresca equivalent stress (MPa)	Maximum Tresca equivalent stress (MPa)
21.86	2.508	40.73	12.32

Table 5. This is due to a very similar in-plane temperature profile in each cell and a negligible temperature gradient through the thickness in each component layer of such a repeated stack configuration. Such a little difference in the steady-state temperature profiles between cells may be attributed to two reasons: (1) the in-plane temperature profile is presumably controlled by the electrochemical reactions and (2) the use of a two-layered ceramic insulation envelope prevents a significant variation of heat loss effect with cell position. However, the differences in the low-stress region pattern from the bottom cell to the middle and top ones may be due to that the constraints from the bottom support condition had more influence on the bottom cell than on the middle and top ones.

3.3. Effect of temperature gradients

In practical operation of an SOFC system, the temperature gradients are inevitably generated by the electrochemical reactions which do not uniformly occur in the SOFC. To understand the contribution of temperature gradients alone to the generation of thermal stress, CTEs of all the SOFC components were assumed the same and equal to that of the PEN in solving the thermal stress distribution. Modeling results indicated considerable thermal stresses were generated by the steady-state temperature gradients alone and the critical stresses for all of the components were listed in Table 6. To make a comparison of thermal stress distribution between the case of considering the steady-state temperature gradients alone and previous results, distributions of MIPPS in the PEN with and without consideration of the CTE mismatch were shown in Fig. 16(a and b), respectively. The corresponding in-plane temperature profile was also given in Fig. 16(c). It is obvious that the thermal stress distribution depended very much on the temperature profile when neglecting the CTE mismatch between components, as shown in Fig. 16(b and c). At the lower-temperature region, it was subjected to tensile stresses which could be attributed to a greater extent of contraction due to a greater temperature difference from the stress-free temperature 800 °C while the higher-temperature region was subjected to compressive stresses. When the CTE mismatch between components was simultaneously taken into account, the location for the greatest MIPPS in the PEN was shifted to the bonding region close to the fuel-inlet end (Fig. 16(a)) and the value was much greater than that for the case only considering the temperature gradients alone (Tables 2 and 6). Therefore, it can be concluded that the CTE mismatch between the PEN and connecting components generated a more significant effect on the thermal stress distribution than did the temperature gradients alone.

3.4. Effect of viscous behavior of glass-ceramic seals

At operation temperature, the glass-ceramic sealant becomes viscous such that thermal stresses might be relaxed to a certain extent. According to the Kelvin model of viscoelasticity [19] for a viscous solid subjected to constant deformation, the completely relaxed load or stress can be characterized by a relaxed elastic modulus. Due to lack of detailed creep and stress relaxation data for G-18 sealant at high temperatures in the literature, a simplified approach was proposed to simulate the viscous behavior of the glass-ceramic sealant at operation temperature by assuming that the elastic modulus of G-18 sealant at 800 °C was eventually relaxed to one-third of the initial value to account for the stress relaxation behavior. Note that in this simplified approach the nonlinear, inelastic stresses were considered non-relaxable. As listed in Table 7, such a simulation of the stress relaxation behavior of G-18 sealant caused a reduction of the critical stress in the PEN, interconnect/frame, and glass-ceramic sealant at steady operation by about 10, 4, and 2%, respectively.

Although the elastic modulus of the glass-ceramic sealant was assumed a reduction of 67% to account for the stress relax-
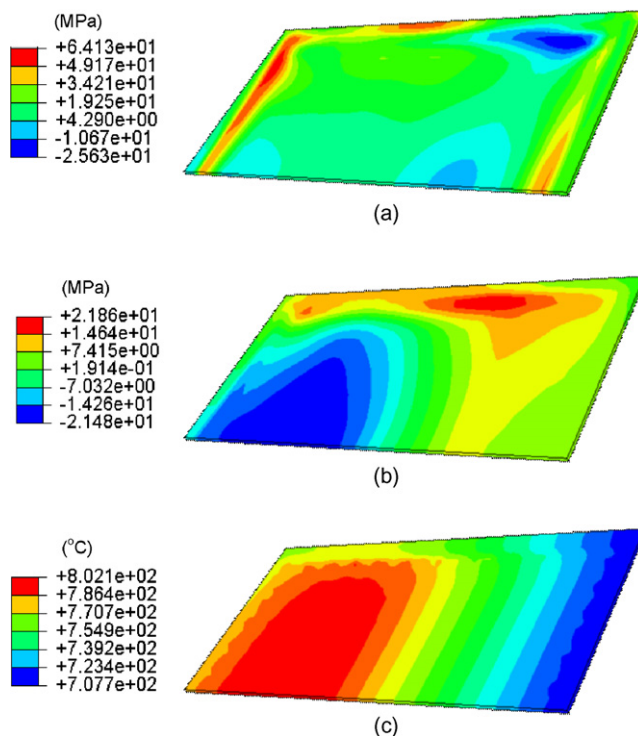

Fig. 16. Distribution of maximum in-plane principal stress in the PEN: (a) with and (b) without consideration of the CTE mismatch effect for edge-support condition. The corresponding in-plane temperature profile is given in (c).

Table 7
Effect of stress relaxation in glass-ceramic sealant on critical stresses

| Condition | PEN | Nickel mesh | IC/frame | Glass-ceramic sealant |
	Maximum in-plane principal stress (MPa)	Maximum Tresca equivalent stress (MPa)	Maximum Tresca equivalent stress (MPa)	Maximum Tresca equivalent stress (MPa)
Unrelaxed	66.82	12.11	83.27	65.72
Relaxed	60.43	12.03	79.77	64.31

ation effect, the amount of reduction in critical stresses in each component was not comparable to this level. This is because the critical state of stress in the glass-ceramic sealant was dominated by inelastic deformation such that only limited elastic strains could be replaced by creep strains during stress relaxation at steady operation. As described in Section 2.2 and Ref. [12], the monotonic stress–strain curve for G-18 became nonlinear at temperatures above 700 °C where inelastic deformation was involved. Microstructural characterization of G-18 sealant after exposure to 800 °C showed existence of crystallized phases embedded in a non-crystallized glassy phase containing a significant number of voids [12]. Therefore, the nonlinear behavior of G-18 at temperatures above 700 °C resulted from viscoelastic behavior of the glassy phase and inelastic deformation [12]. The inelastic deformation was likely to be caused by some reasons: (1) void initiation and growth of existing voids, (2) crystalline/glassy phase decohesion, (3) microcracking, and (4) plasticity of the glassy phase [12]. Knowledge on the creep and stress relaxation properties of the glass-ceramic sealant and advanced analyses with viscoplasticity modeling apparently are needed to further study the effect of viscous behavior of glass-ceramic seals on the thermal stress distribution in SOFCs at steady operation.

3.5. Sensitivity of CTE mismatch between components

As shown in Fig. 4, there are distinguished differences in thermal expansion or CTE mismatch among the PEN, Crofer 22-APU, and G-18 at the temperature range of 600–800 °C so that any temperature change involving this region would cause evident thermal stresses in the SOFC stack. To investigate the effect of CTE mismatch between components, the thermal expansion behaviors of the metallic interconnect/frame and glass-ceramic sealant at this temperature region were modified to be closer to that of the PEN by reducing their thermal expansion in different amounts, as shown in Fig. 17. As described above, the induced thermal stresses in the nickel mesh were not so critical so that its thermal expansion behavior was not made any change in this part of study. The relative thermal expansion of the interconnect/frame at 600–800 °C to that at 600 °C was assumed a reduction of 20% (curve M2) and 40% (curve M3) from the original one (curve M1), as shown in Fig. 17. Similarly, the relative thermal expansion of the glass-ceramic sealant at this temperature range to that at 600 °C was also assumed a reduction of 20% (curve G2) and 40% (curve G3) from the original one (G1), as shown in Fig. 17. Note that curves G1 and M1 represent the unmodified, original thermal expansion behaviors of G-18 and
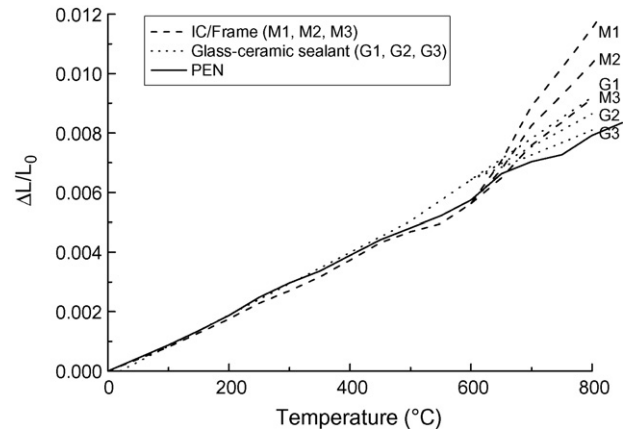

Fig. 17. Modifications of thermal expansion behavior in the interconnect/frame and glass-ceramic sealant with respect to PEN.

Crofer 22-APU, respectively. Table 8 lists the cases investigated under various combinations of these thermal expansion curves.

Table 9 shows the results for the investigated cases listed in Table 8. It can be seen that such modifications of thermal expansion behavior in the metallic interconnect and frame would greatly reduce the thermal stresses generated in the PEN by comparing Cases C and F with Case O in Table 9. However, modifications of thermal expansion behavior in the glass-ceramic sealant would provide only a little reduction of the thermal stresses in the PEN as shown by the results of Cases A and B. Apparently, the thermal expansion behavior of the metallic interconnect and frame had a greater influence on the induced thermal stresses in the SOFC stack than did that of the glass-ceramic sealant. This could be attributed to the fact that interconnects and frames are the dominant parts in a planar SOFC stack in terms of size and volume. When the relative thermal expansion of the interconnect/frame at 600–800 °C was reduced by 20 and

Table 8
Investigated cases for CTE mismatch effect

Case	Involved curves
O (original)	M1 and G1
A	M1 and G2
B	M1 and G3
C	M2 and G1
D	M2 and G2
E	M2 and G3
F	M3 and G1
G	M3 and G2
H	M3 and G3

Table 9
Comparison of critical stresses under various modifications of thermal expansion behavior

Case	Stage	PEN	Nickel mesh	IC/frame	Glass-ceramic sealant	
		Maximum in-plane principal stress (MPa)	Maximum Tresca equivalent stress (MPa)	Maximum Tresca equivalent stress (MPa)	Maximum in-plane principal stress (MPa)	Maximum Tresca equivalent stress (MPa)
O	Shutdown	171.6	17.44	318.5	20.37	–
	Steady-state	66.82	12.11	83.27	–	65.72
A	Shutdown	166.5	17.60	318.7	–25.29	–
	Steady-state	66.71	12.10	82.99	–	66.22
B	Shutdown	167.2	18.32	320.0	–39.97	–
	Steady-state	67.42	12.06	82.51	–	68.74
C	Shutdown	122.7	13.74	321.8	54.75	–
	Steady-state	35.46	8.180	75.12	–	64.91
D	Shutdown	108.3	13.79	321.8	–25.41	–
	Steady-state	34.63	8.165	74.22	–	65.57
E	Shutdown	104.2	13.86	321.8	–55.21	–
	Steady-state	34.03	8.153	73.46	–	65.98
F	Shutdown	57.51	26.69	259.8	96.54	–
	Steady-state	19.33	33.73	46.86	–	35.26
G	Shutdown	54.42	26.77	261.1	41.18	–
	Steady-state	21.17	3.773	46.92	–	45.34
H	Shutdown	51.47	26.91	261.9	–14.00	–
	Steady-state	20.96	3.765	47.00	–	50.94

40%, the greatest MIPPS in the PEN was reduced by 29 and 67%, respectively, at RT and by about 47 and 71%, respectively, at steady operation. Although a reduction of the relative thermal expansion in the interconnect/frame at 600–800 °C alone would greatly reduce the thermal stresses generated in the PEN as seen in Cases C and F, the greatest MIPPS in the glass-ceramic sealant at RT was significantly increased at the same time. In this regard, a reduction of thermal expansion in the glass-ceramic sealant should be simultaneously considered to reduce the tensile stresses in the glass-ceramic sealant at RT.

Cases D, E, G, and H are the cases with simultaneous modifications of thermal expansion in the interconnect/frame and glass-ceramic sealant. As shown in Table 9, for the cases of D and E with an identical thermal expansion in the interconnect/frame but a different one in the glass-ceramic sealant, the corresponding critical stresses in each component were comparable except for the glass-ceramic sealant at the shutdown condition. Similar trends were also found in comparing the results between Cases A and B as well as between Cases G and H. Apparently, when the stack was cooled down from the stress-free temperature to RT (shutdown stage), contraction of the glass-ceramic sealant of curve G3 was less than that of curve G2 such that the greatest MIPPS in the glass-ceramic sealant at RT in each case of B, E, and H was lower than the corresponding one in each case of A, D, and G, respectively. When the relative thermal expansion of the interconnect/frame at 600–800 °C was reduced by 40% (curve M3), results of Cases F, G, and H indicated that the interconnect/frame would deform elastically compared to those cases involving M1 and M2. From these results, it could be concluded that the thermal expansion behavior of the interconnect/frame affected the thermal stress distribution in the PEN more than

did that of the glass-ceramic sealant. This was due to a domination of the interconnect/frame in the volume of a planar SOFC assembly. In other words, development of a metallic interconnect/frame material with a thermal expansion behavior as close as possible to that of the PEN would be more effective in reducing the thermal stresses in a SOFC stack than the modification of thermal expansion behavior in glass-ceramic sealants for the given SOFC stack design.

4. Conclusions

A 3D FEA model of a three-cell stack based on a prototype planar SOFC stack design was constructed in the current study to perform thermal stress analyses at shutdown, start-up, and steady-state stages. Effects of bottom support condition, cell position, temperature gradients, viscous behavior of the glass-ceramic sealant, and CTE mismatch sensitivity were investigated and simulation results were summarized as follows:

(1) Edge-, plane-, and point-support at bottom frame generated comparable thermal stress distributions, as only the bottom frame was constrained in different ways and similar constraints were set on the other corresponding components in the three-cell SOFC stack under different support conditions.

(2) At room temperature (shutdown stage), the calculated thermal stresses in the PENs, interconnects/frames, and glass-ceramic sealants were lower than the corresponding fracture strength while localized plastic deformation in the interconnects/frames was predicted. At steady operation, localized plastic deformation was also predicted for the

interconnects/frames and predictions of the maximum shear stress in glass-ceramic sealants were greater than the shear strength of G-18 sealant.

(3) The critical stresses in each corresponding component of the top, middle, and bottom cells in the three-cell stack were comparable. This was due to a resemblance of the in-plane temperature profiles and a negligible out-of-plane temperature gradient.

(4) The CTE mismatch effect generated a greater extent of influence on the thermal stress distribution in the SOFC than did the temperature gradients alone. Making the thermal expansion behavior of the interconnect/frame closer to that of the PEN could effectively reduce the thermal stresses generated in the PEN as well as in the interconnect/frame. However, a similar modification for the glass-ceramic sealant was less effective in reducing the thermal stresses in the PEN or interconnect/frame.

(5) With an assumption of relaxation of the elastic modulus of G-18 sealant at 800 °C by 67% to account for the stress relaxation effect of the viscous glass-ceramic sealants at steady operation, the greatest maximum in-plane principal stress in the PEN was reduced by about 10%. However, the greatest Tresca equivalent stress in the glass-ceramic sealants and interconnects/frames was only relaxed by a small amount because only limited elastic strains were relaxed in these components.

Based on the simulation results described above, the glass-ceramic sealant apparently is the most critical part of the prototype planar SOFC stack investigated, in particular at operation temperature where failure of such a component was predicted. As for the metallic interconnect and frame, they might be acceptable depending on how much localized plastic deformation is allowed. Therefore, commercialization of such a planar SOFC stack under the current conditions is obviously not possible in terms of structural reliability. As described in Section 1, glass-ceramic seals were never considered in the literature [1–8] on modeling of thermal stress distribution in planar SOFCs. However, the simulation results in the current study did point out the important role of the glass-ceramic sealant in the structural reliability of a planar SOFC stack which should not be neglected in any thermal stress analysis for a practical SOFC system. Apparently, glass-ceramic sealants in planar SOFCs not only need to provide necessary adherence, electric insulation, chemical stability and compatibility but also need to survive mechanical degradation during operation. Further studies on the thermal stress analysis of planar SOFCs should pay more attention to the viscous behavior of glass-ceramic sealants. In particular, extended knowledge of the high-temperature mechanical properties of glass-ceramic sealants such as creep, stress relaxation, viscoelasticity and/or viscoplasticity is necessary. In this way, the FEA model can be enhanced and more precisely account for the viscous effect of the glass-ceramic sealant on thermal stress distributions at steady operation so as to provide more practical simulation results for design and development of highly efficient and reliable planar SOFCs.

Acknowledgement

References

[1] A. Selcuk, G. Merere, A. Atkinson, J. Mater. Sci. 36 (2001) 1173–1182.
[2] C.S. Montross, H. Yokokawa, M. Dokiya, Br. Ceram. Trans. 101 (2002) 85–93.
[3] H. Yakabe, Y. Baba, T. Sakurai, M. Satoh, I. Hirosawa, Y. Yoda, J. Power Sources 131 (2004) 278–284.
[4] H. Yakabe, Y. Baba, T. Sakurai, Y. Yoshitaka, J. Power Sources 135 (2004) 9–16.
[5] W. Fischer, J. Malzbender, G. Blass, R.W. Steinbrech, J. Power Sources 150 (2005) 73–77.
[6] H. Yakabe, T. Ogiwara, M. Hishinuma, I. Yasuda, J. Power Sources 102 (2001) 144–154.
[7] A. Selimovic, M. Kemm, T. Torisson, M. Assadi, J. Power Sources 145 (2005) 463–469.
[8] A. Nakajo, C. Stiller, G. Harkegard, O. Bolland, J. Power Sources 158 (2006) 287–294.
[9] Y.P. Chyou, T.D. Chung, J.S. Chen, R.F. Shie, J. Power Sources 139 (2005) 126–140.
[10] ABAQUS Analysis User's Manual, vol. IV: Elements, Version 6.5, ABAQUS Inc., Providence, RI, USA, 2004, pp. 15.6.1-1–15.6.10-5.
[11] K.S. Weil, J.E. Deibler, J.S. Hardy, D.S. Kim, G.-G. Xia, L.A. Chick, C.A. Coyle, J. Mater. Eng. Perform. 13 (2004) 316–326.
[12] B.N. Nguyen, B.J. Koeppel, S. Ahzi, M.A. Khallel, P. Singh, J. Am. Ceram. Soc. 89 (2006) 1358–2368.
[13] N.P. Bansal, E.A. Gamble, J. Power Sources 147 (2005) 107–155.
[14] W. Koster, Z. Metallkd. 39 (1948) 1–9.
[15] Metals Handbook, vol. 2, 10th ed., ASM International, Materials Park, OH, USA, 1990, pp. 437–441.
[16] J. Malzbender, R.W. Steinbrech, L. Singhesier, in: N.P. Bansal (Ed.), Advances in Solid Oxide Fuel Cells, The American Ceramic Society, Westerville, OH, USA, 2005, pp. 293–298.
[17] J.A. Collins, Failure of Materials in Mechanical Design: Analysis, Prediction, Prevention, second ed., John Wiley & Sons, New York, 1993, pp. 144–146.
[18] N.P. Bansal, J.B. Hurst, S.R. Choi, J. Am. Ceram. Soc. 89 (2006) 388–390.
[19] Y.C. Fung, P. Tong, Classical and Computational Solid Mechanics, World Scientific Publishing Co. Pte. Ltd., Singapore, 2001, pp. 9–12.